



HAL
open science

Imaging with cross-hole seismoelectric tomography

A. H. Araji, A. Revil, Abderrahim Jardani, B.J. Minsley, M. Karaoulis

► **To cite this version:**

A. H. Araji, A. Revil, Abderrahim Jardani, B.J. Minsley, M. Karaoulis. Imaging with cross-hole seismoelectric tomography. *Geophysical Journal International*, 2012, 188, pp.1285-1302. 10.1111/j.1365-246X.2011.05325.x . hal-00734724

HAL Id: hal-00734724

<https://hal.science/hal-00734724>

Submitted on 18 Jun 2021

HAL is a multi-disciplinary open access archive for the deposit and dissemination of scientific research documents, whether they are published or not. The documents may come from teaching and research institutions in France or abroad, or from public or private research centers.

L'archive ouverte pluridisciplinaire **HAL**, est destinée au dépôt et à la diffusion de documents scientifiques de niveau recherche, publiés ou non, émanant des établissements d'enseignement et de recherche français ou étrangers, des laboratoires publics ou privés.

Imaging with cross-hole seismoelectric tomography

A. H. Araj, ¹ A. Revil, ^{1,2} A. Jardani, ⁴ B. J. Minsley ⁴ and M. Karaoulis ¹

¹Colorado School of Mines, Dept. of Geophysics, Golden, CO 80401, USA

²ISTerre, CNRS, UMR 5559, Université de Savoie, Equipe Volcan, Le Bourget du Lac, France. E-mail: arevil@mines.edu

³Université de Rouen, M2C, UMR 6143, CNRS, Morphodynamique Continentale et Côtière, Mont Saint Aignan, France

⁴US Geological Survey, Crustal Geophysics and Geochemistry Science Centre, MS964-Denver Federal Centre, Denver, CO 80225, USA

Accepted 2011 November 29. Received 2011 November 21; in original form 2011 February 9

SUMMARY

We propose a cross-hole imaging approach based on seismoelectric conversions (SC) associated with the transmission of seismic waves from seismic sources located in a borehole to receivers (electrodes) located in a second borehole. The seismoelectric (seismic-to-electric) problem is solved using Biot theory coupled with a generalized Ohm's law with an electrokinetic streaming current contribution. The components of the displacement of the solid phase, the fluid pressure, and the electrical potential are solved using a finite element approach with Perfect Match Layer (PML) boundary conditions for the seismic waves and boundary conditions mimicking an infinite material for the electrostatic problem. We develop an inversion algorithm using the electrical disturbances recorded in the second borehole to localize the position of the heterogeneities responsible for the SC. Because of the ill-posed nature of the inverse problem (inherent to all potential-field problems), regularization is used to constrain the solution at each time in the SC-time window comprised between the time of the seismic shot and the time of the first arrival of the seismic waves in the second borehole. All the inverted volumetric current source densities are aggregated together to produce an image of the position of the heterogeneities between the two boreholes. Two simple synthetic case studies are presented to test this concept. The first case study corresponds to a vertical discontinuity between two homogeneous sub-domains. The second case study corresponds to a poroelastic inclusion (partially saturated by oil) embedded into an homogeneous poroelastic formation. In both cases, the position of the heterogeneity is recovered using only the electrical disturbances associated with the SC. That said, a joint inversion of the seismic and seismoelectric data could improve these results.

Key-words Electrical properties; Hydrogeophysics; Permeability and porosity.

1 INTRODUCTION

The seismoelectric method is an active geophysical method that consists of measuring the electromagnetic excitations associated with the conversion of the mechanical energy of seismic waves into electromagnetic energy at macroscopic interfaces characterized by variation in the electrical, hydraulic, and/or mechanical properties. This interface conversion is often referred to as the seismoelectric conversion (SC) in the geophysical literature. Another type of electrical signal is the coseismic electrical signal propagating with the seismic waves themselves. The seismoelectric method has been used mainly in geophysical exploration (Martner & Sparks 1959; Migunov & Kokorev 1977; Kopic *et al.* 1995; Russel *et al.* 1997) but it is also a potential tool to image glaciers (Kulesa *et al.* 2006), shallow objects (Haines *et al.* 2007), and the position of the water table (Dupuis *et al.* 2007). The seismoelectric method is mainly used as a surface geophysical method. However, this method has also been used in boreholes, as a logging tool, especially for the

detection of fractures and high permeability flow pathways (Zhu & Toksöz 1998, Zhu *et al.* 1999; Mikhailov *et al.* 2000; Dupuis & Butler 2006; Hu *et al.* 2007; Dupuis *et al.* 2009) or for cross-hole measurements as demonstrated by Zhu & Toksöz (2003). The seismoelectric method is also used to characterize the texture of porous media (including colloidal suspensions) in the laboratory (e.g. Zhu *et al.* 2008; Dukhin & Shilov 2010).

One of the challenges in the seismoelectric method is that it may be difficult to distinguish between SC and coseismic signals (e.g. Haines 2004). These coseismic signals are associated with the relative displacement between the pore water (dragging the diffuse part of the electrical double layer coating the surface of the grains) and the solid phase (Haartsen & Pride 1997). The magnitude of this drag is frequency-dependent. Zhu & Toksöz (2003) and Haines *et al.* (2007) proposed to separate the seismic sources from the electrical receivers in order to temporally separate the SC from the co-seismic signals. To avoid to separate the coseismic signals from the SC, Jardani *et al.* (2010) have recently developed a stochastic

full-waveform inversion of surface low-frequency seismoelectric and seismic data to determine the probability distribution of the material properties of different geological units. In their approach, Jardani *et al.* (2010) assumed that the position of the discontinuities is independently known and both the seismic, seismoelectric and coseismic signals waveforms are used to invert the electrical, hydraulic, and mechanical properties. In this paper, we take the complementary approach and our objective below is to image the position and shape of the heterogeneities between two boreholes regardless the value of the material properties. In such a case, we can use only the SC signals, avoiding the coseismic signals, because the SC arrive earlier than the co-seismic signals in the second borehole Zhu & Toksöz (2003) and Haines *et al.* (2007). Going one step further and inverting for both the material properties and geometry simultaneously will be an area of future research.

2 BACKGROUND THEORY

In this section, we describe the equations that are used to model the seismoelectric problem. We present these equations for two reasons: (1) the poroelastic formulation we use is distinct from the poroelastic formulation used by previous researchers working on the seismoelectric problem and (2) the electrokinetic formulation we use is also different than the electrokinetic formulation used by previous researchers in modelling the seismoelectric signals.

2.1 Poroelastic equations

In this section, we review first the basic equations of linear poroelasticity in an isotropic porous material and we provide the motivation for using the fluid pressure and the displacement components of the solid phase as state variables rather than the displacement components of the water and solid phases. In our model, the wave equations in a water-saturated isotropic linear poroelastic body are described by Frenkel-Biot's theory (Frenkel 1944; Biot 1962a,b). This theory describes the propagation of two (compressional) P waves (the fast and slow P waves) and the (shear) S waves in a water-saturated porous body. The governing equations (including an inertial term in the Navier-Stokes equations) for this problem are Newton's law, Hooke's law, Darcy's law, and some of the Biot's constitutive equations. Because we solve these equations in the frequency domain using a fine element approach, we provide these equations in the frequency domain (see Pride 1994; Karpfinger *et al.* 2009; Gao & Hu 2010),

$$-\omega^2 (\rho \mathbf{u} + \rho_f \mathbf{w}) = \nabla \cdot \mathbf{T} + \mathbf{F}, \quad (1)$$

$$\mathbf{T} = [\lambda_u \nabla \cdot \mathbf{u} + C \nabla \cdot \mathbf{w}] \mathbf{I} + G[\nabla \mathbf{u} + \nabla \mathbf{u}^T] \quad (2)$$

$$-\omega^2 (\rho_f \mathbf{u} + \tilde{\rho}_f \mathbf{w}) - j b \omega \mathbf{w} = -\nabla p + \mathbf{F}_f, \quad (3)$$

$$-p = C \nabla \cdot \mathbf{u} + M \nabla \cdot \mathbf{w}, \quad (4)$$

where $j^2 = -1$ (j represents the pure imaginary number), $\omega = 2\pi f$ is the angular frequency in rad s^{-1} (f is the frequency in Hz), \mathbf{u} denotes the solid displacement vector (in m), while \mathbf{w} (in m) denotes the fluid vector displacement relative to the solid (in a Lagrangian framework of reference associated with the deformation of the solid), \mathbf{F} is the body force on the elastic solid phase (in N), and \mathbf{F}_f is the body force on the viscous fluid phase (in N). The matrix \mathbf{I} represents the identity matrix, ρ represents the mass density of the saturated porous medium (in kg m^{-3}), and ρ_f and ρ_s denotes fluid

mass density and the solid mass density respectively (in kg m^{-3}). The apparent density $\tilde{\rho}_f$ (in kg m^{-3}) denotes an apparent density of the fluid including inertial effects (defined later), \mathbf{T} is the total stress tensor (in Pa), p denotes the pore fluid pressure (in Pa), $\lambda_u = K_u - (2G/3)$ denotes the undrained Lamé modulus of the porous material (in Pa), b denotes the mobility of the fluid in the porous material (defined later and expressed in Pa s m^{-2}), G represents the shear modulus of the porous frame (in Pa), and C and M are of the Biot Moduli (in Pa). Eq. (1) represents Newton's second law (a momentum conservation equation for the porous material), eq. (2) represents Hooke's constitutive law for the stress-strain relationship, eq. (3) is Darcy's law (momentum conservation equation for the fluid), and eq. (4) represents one of Biot's constitutive equation of linear poroelasticity.

The other material properties entering eqs (1)–(4) are given by

$$\rho = \phi \rho_f + (1 - \phi) \rho_s, \quad (5)$$

$$b = \frac{\eta_f}{k_0}, \quad (6)$$

$$\tilde{\rho}_f = \frac{\rho_f}{F}, \quad (7)$$

$$\alpha = 1 - K_{fr}/K_s, \quad (8)$$

$$K_u = \frac{K_f(K_s - K_{fr}) + \phi K_{fr}(K_s - K_f)}{K_f(1 - \phi - K_{fr}/K_s) + \phi K_s}, \quad (9)$$

$$C = \frac{K_f(K_s - K_{fr})}{K_f(1 - \phi - K_{fr}/K_s) + \phi K_s}, \quad (10)$$

$$M = \frac{C}{\alpha} = \frac{K_f K_s}{K_f(1 - \phi - K_{fr}/K_s) + \phi K_s}, \quad (11)$$

where K_u represents the bulk (undrained) modulus of the porous medium (in Pa), K_{fr} represents the bulk modulus of the dry porous frame (in Pa), K_f is bulk modulus of the pore fluid (in Pa), K_s denotes the bulk modulus of the solid phase (in Pa), α is the Biot-Willis Coefficient (dimensionless), η_f denotes the dynamic viscosity of the pore fluid (in Pa s), k_0 denotes the DC-permeability (in m^2), ϕ denotes the connected porosity (dimensionless), and F (dimensionless) denotes the electrical formation factor, which is the ratio between the bulk tortuosity of the pore space divided by the connected porosity. In the following, we use Archie's law to compute the formation factor $F = \phi^{-m}$, with m , the cementation exponent, equals to 2 in clayey sandstones (Archie 1942; Revil *et al.* 1998)

The previous set of equations are usually used to solve the seismic problem for the three components of \mathbf{u} and the three components of \mathbf{w} in 3-D. However the poroelastic problem can be written in term of the displacement of the solid phase \mathbf{u} and the fluid pressure reducing the number of unknowns from 6 to 4 in 3-D and from 4 to 3 for 2.5D and 2-D problems. Indeed, eqs (1)–(4) can be written as (e.g. Jardani *et al.* 2010 and references therein):

$$-\omega^2 \rho_\omega^s \mathbf{u} + \theta_\omega \nabla p = \nabla \cdot \hat{\mathbf{T}} + \mathbf{F}, \quad (12)$$

$$\hat{\mathbf{T}} = \lambda(\nabla \cdot \mathbf{u}) \mathbf{I} + G[\nabla \mathbf{u} + \nabla \mathbf{u}^T], \quad (13)$$

$$\frac{1}{M} p + \nabla \cdot \{k_\omega [\nabla p - \omega^2 \rho_f \mathbf{u}]\} = \alpha \nabla \cdot \mathbf{u}. \quad (14)$$

In 2-D, this change of variables reduces the number of variables from 4 (u_x, u_z, w_x, w_z) to three (p, u_x, u_z). This is very important to reduce the computational power needed to solve the forward problem. The relationship between the total stress tensor and the effective stress tensor $\hat{\mathbf{T}}$ is $\mathbf{T} = \hat{\mathbf{T}} - \alpha p \mathbf{I}$. The material properties entering into equations (12)–(14) are given by Jardani *et al.* (2010):

$$k_\omega = \frac{1}{\omega^2 \tilde{\rho}_f + j\omega b}, \quad (15)$$

$$\lambda = K_{fr} - \frac{2}{3}G, \quad (16)$$

$$\rho_\omega^s = \rho - \omega^2 \rho_f^2 k_\omega, \quad (17)$$

$$\theta_\omega = \alpha - \omega^2 \rho_f k_\omega, \quad (18)$$

where k_ω is a frequency-dependent transfer function, $\tilde{\rho}_f$ is an effective fluid density, λ is the (drained) Lamé coefficient (in Pa), and ρ_ω^s corresponds to the apparent mass density of the solid phase at a given frequency ω (in kg m^{-3}). The exact form of the partial differential equations to solve are given in Jardani *et al.* (2010) and will not be repeated here.

Assuming that the viscous coupling can be neglected, the velocity of the P waves, c_p , and the velocity of the shear waves, c_s , are approximated by the Biot–Gassmann equations (Gassmann 1951),

$$c_p^2 = \frac{K_u + \frac{4G}{3}}{\rho} = \frac{H}{\rho}, \quad (19)$$

$$c_s^2 = \frac{G}{\rho}. \quad (20)$$

Eqs (19) and (20) can be used to get a first estimate of the traveltimes of the different waves through the porous body as shown later. The compressional modulus H in eq. (19) is defined by

$$H = \frac{(K_s - K_{fr})^2}{D - K_{fr}} + K_{fr} + \frac{4}{3}G, \quad (21)$$

$$D = K_s \left[1 + \phi \left(\frac{K_s}{K_f} - 1 \right) \right]. \quad (22)$$

More elaborate velocity relationships can be found in Morency & Tromp (2008) in the case where the viscous coupling is not negligible. These relationships take into account the frequency dependence of the seismic waves.

2.2 The Seismic source

The force associated with the seismic source described by the moment tensor \mathbf{M} is given by (e.g. Dahlen & Tromp 1998; Morency & Tromp 2008),

$$\mathbf{F} = -\mathbf{M} \cdot \nabla \delta(\mathbf{r} - \mathbf{r}_s) S(t), \quad (23)$$

where \mathbf{r}_s refers to the point source location, $\delta(\mathbf{r} - \mathbf{r}_s)$ is the Dirac delta distribution located at \mathbf{r}_s , and $S(t)$ is the source time function. We consider an explosion generating compressional P waves only. We use a Gaussian pulse to simulate the explosion. In the frequency domain, the force associated with the source is therefore given by Lathi (1998):

$$\mathbf{F}(x, y, \omega) = F(\omega) \delta(x - x_0) \delta(y - y_0), \quad (24)$$

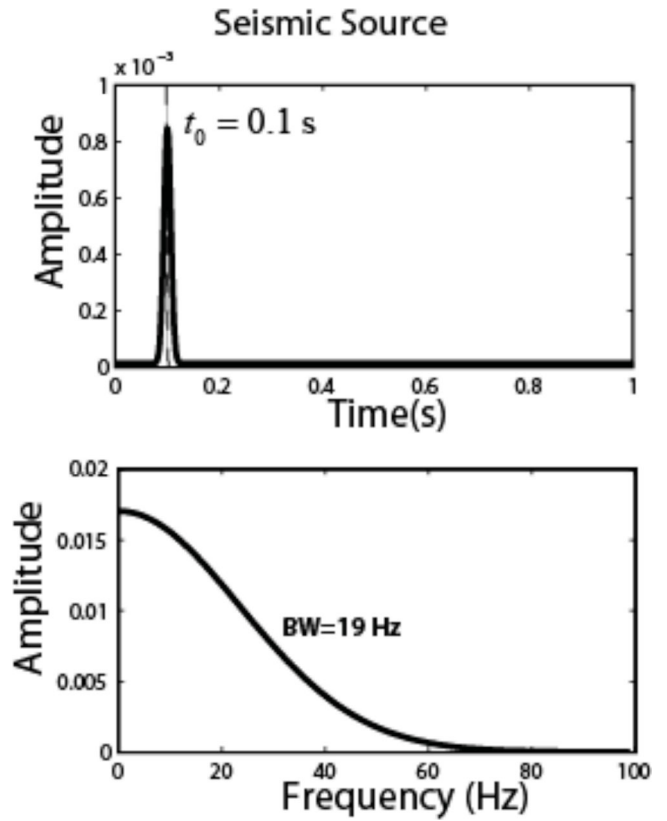


Figure 1. Description of the seismic explosive source. We use a sharp Gaussian pulse simulating an explosion at $t_0 = 0.1$ s. The standard deviation of the source in the frequency domain is 19 Hz.

$$F(\omega) = \sigma_p \sqrt{2\pi} e^{-\frac{\sigma_p^2 \omega^2}{2}} e^{-j\omega t_0}, \quad (25)$$

where x_0 and z_0 denote the position of the source, $F(\omega) = \text{FT}[f(t)]$ is the Fourier transform of the argument $f(t) = \exp(-(t - t_0)^2 / 2\sigma_p^2)$, and σ_p is the variance of the pulse in the time domain. In the following, we use $t_0 = 0.1$ s for the time delay and a standard deviation of 19 Hz (Fig. 1). Because seismic sources rarely have any energy at zero frequency, we rarely model them as Gaussian waveforms. We can use the 1st or 2nd derivative of a Gaussian (the negative of the latter corresponds to a “Ricker wavelet” source). That said, we point out that the results of the following models are strictly independent of the choice of the source as long as the source is known. Indeed, it is always possible to perform a deconvolution of the seismoelectric response from the time dependence of the source to obtain the response associated with an impulse function.

2.3 The electrical signals

The electrokinetic coupling in the seismoelectric response is the result of a relative displacement of the pore water with respect to the solid phase. We use below the electrokinetic theory developed by Revil and co-workers (Revil *et al.* 2005, Revil & Linde 2006, and Revil 2007). This approach was used by Bolève *et al.* (2007) and Crespy *et al.* (2008) to solve some hydrogeophysical problems and Jardani *et al.* (2010) and Revil & Jardani (2010) to solve some seismoelectric problems and this theory has already been extended to

unsaturated conditions by Revil *et al.* (2007). Three approximations are made to determine the seismoelectric disturbances:

(1) The transport of the electromagnetic disturbances is diffusive by nature for the low-frequency range we are interested in. As we are dealing with characteristic distances of few hundred meters, the electromagnetic problem can be solved in the quasi-static limit of the Maxwell equations. We justify as follows the fact that we can neglect the characteristic time of diffusion of the electromagnetic disturbances between the areas where a SC occurs and the receivers. The electromagnetic diffusivity is defined by $\eta = 1/\mu\sigma$ where μ is the magnetic permeability (in H m^{-1}). From the dimensional analysis of the electromagnetic diffusivity, the characteristic time of diffusion is $\tau = L^2/\eta = L^2\mu\sigma$ where L is a characteristic distance between the source and a receiver. Taking $\mu = 10^{-6} \text{ H m}^{-1}$, $\sigma = 0.001 \text{ S m}^{-1}$, and $L = 300 \text{ m}$, we obtain $\tau = 0.1 \text{ ms}$. Therefore the electromagnetic information diffuses much faster than the seismic information travels (the traveltime for the seismic information is on the order of 200 ms). So we can safely neglect the diffusion of the electromagnetic disturbances associated with the SC and we can consider the problem in the quasi-static limit of the Maxwell equations (Jardani *et al.* 2010, and Revil & Jardani 2010).

(2) Rather than using the classical electrokinetic theory based on the 'zeta potential' at the pore water solid interface (e.g. Pride 1994; Revil *et al.* 1999; Revil & Leroy 2004), our model is based on an effective excess of electrical charge density in the pore water, \bar{Q}_V . This approach offers an alternative to Pride (1994) theory used in most recent papers dealing with the forward modelling of the seismoelectric response of porous rocks (e.g. Garambois & Dietrich 2002). The charge density \bar{Q}_V is defined as the volume average of the product of the local charge density by the local relative velocity of the pore water divided by the average velocity of the pore water. This approach allows to reduce the number of variables used to describe the streaming current density as the effective charge density per unit pore volume is strongly correlated to the permeability of the porous material (Revil & Jardani 2010).

(3) We neglect the electromagnetic disturbances directly related to the seismic source itself (for electromagnetic effects associated with the source, see Huang 2002, Haines 2004, and Huang & Liu 2006). While these signals can be observed in field conditions, they only provide an information on the time of the source and the potential distribution depends on the resistivity distribution between the source and the electrodes.

Under the quasi static limit of the Maxwell equations, the electrical potential ψ (in V) is governed by the following Poisson equation:

$$\nabla \cdot (\sigma \nabla \psi) = \nabla \cdot \mathbf{j}_S, \quad (26)$$

where the source current density \mathbf{j}_S (in A m^{-2}) is defined as (Jardani *et al.* 2010, Revil & Jardani 2010):

$$\mathbf{j}_S = \bar{Q}_V \dot{\mathbf{w}} = -j\omega \bar{Q}_V k_\omega (\nabla p - \omega^2 \rho_f \mathbf{u}), \quad (27)$$

where $\mathbf{E} = -\nabla \psi$ is the (quasi-static) electrical field (in V m^{-1}), σ denotes the electrical conductivity of the porous rock (in S m^{-1}), \mathbf{j}_S denotes a source current density of electrokinetic nature (in A m^{-2}), and \bar{Q}_V (in C m^{-3}) denotes the excess of electrical charges of the diffusive layer per unit pore volume for the saturated rock. The volumetric source term in the right-hand-side of eq. (26), defined as

$$\mathfrak{S}(\mathbf{r}, t) = \nabla \cdot \mathbf{j}_S(\mathbf{r}, t), \quad (28)$$

(expressed in A m^{-3}), is associated with the seismic wave propagation. It is a function of both space and time. Any heterogeneity

associated with the variables involved in eq. (27) can be responsible for a source current density and the divergence of this current source density, eq. (28), can be, in turn, responsible for an electrical field. The volumetric source current density varies both on space and time at positions where heterogeneities are illuminated by the propagation of the seismic waves as shown in the next section.

2.4 Boundary conditions at an interface

If we consider an interface between two media 1 and 2, the boundary conditions at the interface are given by Pride & Haartsen (1996):

$$\mathbf{u}_1 = \mathbf{u}_2, \quad (29)$$

$$p_1 = p_2, \quad (30)$$

$$\hat{\mathbf{n}} \cdot (\mathbf{w}_1 - \mathbf{w}_2) = 0, \quad (31)$$

$$\hat{\mathbf{n}} \cdot (\mathbf{T}_1 - \mathbf{T}_2) = 0, \quad (32)$$

$$\hat{\mathbf{n}} \times (\mathbf{E}_1 - \mathbf{E}_2) = 0, \quad (33)$$

where $\hat{\mathbf{n}}$ is the unit vector normal to the interface between the media 1 and 2. These boundary conditions express the continuity in the solid displacement, the pore fluid pressure, the fluid displacement, the momentum flux, and the tangential components of the electrical field across the interface.

2.5 Lateral resolution of cross-hole seismoelectric data

In seismic, the first seismic Fresnel zone is defined as the area of the reflector that contributes constructively energy to the total reflection energy reaching an observation point P. The same definition can be used for the transmission problem. In our case, the seismoelectric Fresnel zones may be defined similarly as the area of an interface that contributes constructively to the total transmitted energy reaching an observation point P. If we consider a monochromatic seismic source S located above a horizontal interface between media of different electrical properties, the spherically spreading seismic wave intersects the interface and causes fluid flow across the interface. The resulting electrical field is due to the streaming current imbalance at the interface. This is equivalent to have electrical dipoles oscillating in phase with the seismic wave along the interface. As a consequence, electromagnetic disturbances are radiated away from the dipole sources and are recorded at the observation point P. Assuming that S and P are collocated, the first Fresnel zones correspond to two circles of radii r_S and r_{SE} , respectively. Fourie (2003) provided a complete analysis of the reflection problem and found that the seismic and seismoelectric first Fresnel zone radii are given by

$$r_S = \left[\left(d + \frac{\lambda_S}{4} \right)^2 - d^2 \right]^{1/2} \approx \sqrt{d\lambda_S/2}, \quad (34)$$

$$r_{SE} = \left[\left(d + \frac{\lambda_S}{2} \right)^2 - d^2 \right]^{1/2} \approx \sqrt{d\lambda_S}, \quad (35)$$

respectively, where d denotes the distance between S and the interface and λ_S corresponds to the wavelength of the seismic wave. The approximation in eqs (34) and (35) are obtained by assuming that $d \gg \lambda_S$ and it yields $r_{SE} \approx \sqrt{2}r_S$. In eq. (35), it is

further assumed that the diffusion of the electromagnetic disturbances is much faster than the propagation of the seismic energy, a very good approximation as discussed above in Section 2.3. Therefore the lateral resolution of surface seismoelectric data is poorer when compared with the lateral resolution of surface seismic data. Fourie (2003) showed also that for a horizontal interface the first seismoelectric Fresnel zones is nearly circular and centered beneath the shot-point S. For the seismic case, the first Fresnel zone is an ellipse centered halfway between the shot-point and the observation point P.

3 FORWARD MODELLING OF THE SYNTHETIC DATA

The forward seismoelectric problem is performed with the finite-element package COMSOL Multi-physics 3.5a and we use the same partial differential equations as Jardani *et al.* (2010). The problem specification in COMSOL comprises the following steps: (1) formulating the semi-coupled field equations describing the dynamic poroelastic problem and the associated electromagnetic disturbances (see Section 2 earlier), (2) defining the geometry of the model (see Fig. 2), (3) specifying the model parameters (see Tables 1 and 2), (4) designing the finite element mesh (we use triangular meshing in the present case), (5) selecting the boundary layer conditions (we use PML boundary conditions for the seismic problem, see Fig. 2), (6) solving the partial differential field equations, (7) performing the inverse quasi-electrostatic problem, and finally (8) post-processing the data to produce an image using a pixel-based approach. The flow chart is shown in Fig. 3. The PML

boundary conditions consist of a strip simulating the propagation of the seismic waves into free space without any reflections going back inside the domain of interest (see Jardani *et al.* 2010 for further details on the implementation).

The first problem is to simulate the seismic wave propagation associated with the source in order to get the distribution of the two components of the displacement along the coordinates x and z and the mean pore fluid pressure p at each time t . Since we are solving stationary partial differential equations in the frequency domain, we use the stationary parametric solver PARDISO (<http://www.pardiso-project.org/>, see also Bollhoefer *et al.* 2009). This solver is used to determine the distribution of the following parameters: first, the fields u_x, u_z, p are determined as a function of space and time using a back-Fourier transform of the solution in the spatial and temporal frequency domain, and then the quasi-static scalar potential ψ is computed by solving the Poisson equation coupled to the solution of u_x, u_z, p by its source term. The solution in the time domain is computed using an inverse-Fourier transform. In the frequency domain, we solve the partial differential equations from 1 to 100 Hz with a step of 1 Hz. The seismic forward modelling code we used has been benchmarked by Jardani *et al.* (2010) using the analytical solution of Dai *et al.* (1995) for a water-saturated poroelastic material. Then, we use the components of the solid displacement and the fluid pressure to determine the electrical potential distribution at each time step. In our modelling, we will also neglect the Stoneley waves propagating along the boreholes in which the seismic sources are located. These Stoneley waves can generate seismoelectric signals (Mikhailov *et al.* 2000; Hunt & Worthington 2000) and should be considered in the case of a real field experiment. However, we believe that they can be easily filtered out of the recorded

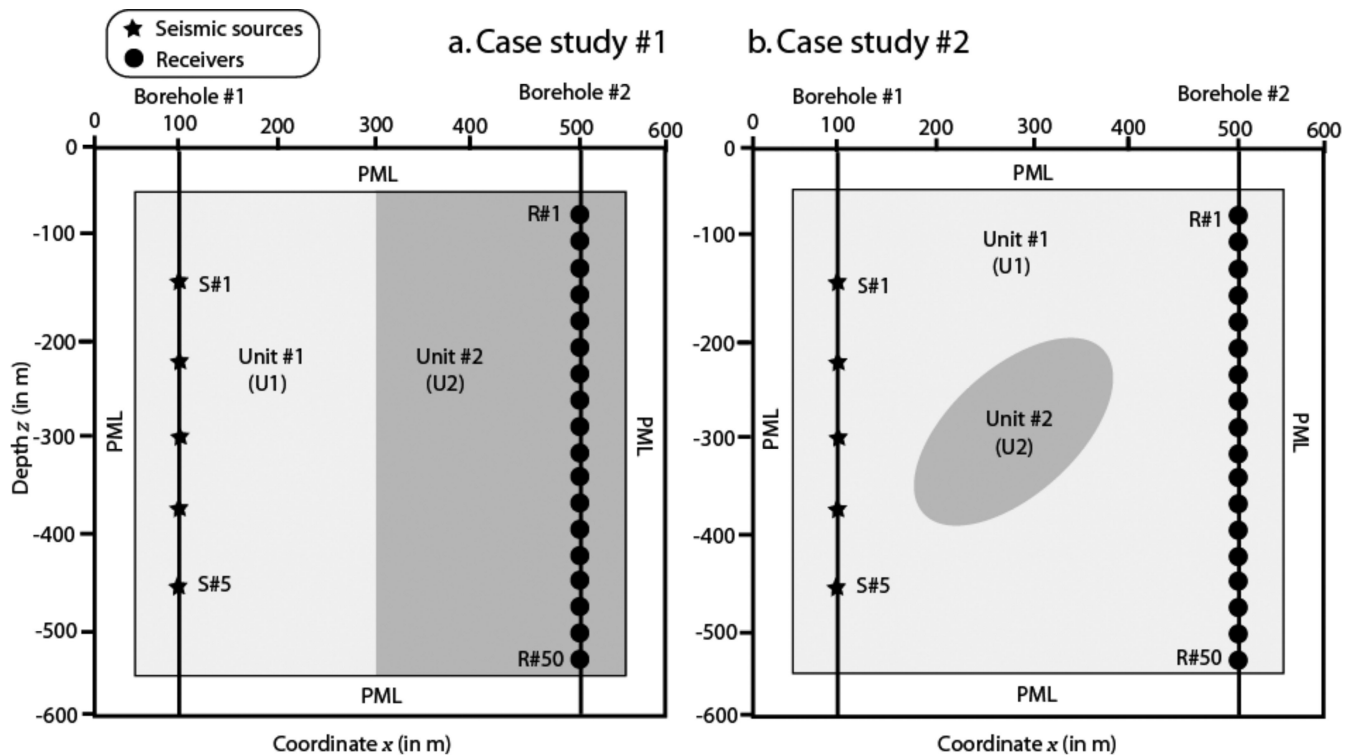


Figure 2. The domain is a 600 m × 600 m square. Borehole, #1, the shooting borehole, is located at position $x = 100$ m and the measurement borehole, #2, is located at $x = 500$ m. The discretization of the domain comprises a finite element mesh of 60×60 rectangular cells. We consider 5 seismic sources (from S#1 at the top to S#5 at the bottom) equally spaced in Borehole #1 and 50 receivers (R#1 to R#50 at the bottom) located in Borehole #2. PML boundary conditions are used at the borders of the domain. a. The Case Study #1 concerns a vertical interface separating two homogeneous half-space. This interface is located at $x = 300$ m, at equal distance between the two sources. b. The Case Study #2 corresponds to an inclusion U2 embedded into a homogeneous material U1.

Table 1. Material properties used for the numerical simulations corresponding to the case study #1. Unit U1 simulates a sandstone and unit U2 is used to simulate a clayey sandstone.

| Parameter | Description | Unit U1 | Unit U2 |
|-------------|---------------------------------------|----------------------------------|----------------------------------|
| σ | Conductivity of the medium | 0.01 S m ⁻¹ | 0.1 S m ⁻¹ |
| \bar{Q}_V | Excess of charge per unit pore volume | 0.203 C m ⁻³ | 3.49 C m ⁻³ |
| ρ_s | Bulk density of the solid phase | 2650 kg m ⁻³ | 2650 kg m ⁻³ |
| ρ_f | Bulk density of the fluid phase | 1000 kg m ⁻³ | 1000 kg m ⁻³ |
| ϕ | Porosity | 0.25 | 0.10 |
| K_s | Bulk modulus of the solid phase | 36.5 × 10 ⁹ Pa | 6.9 × 10 ⁹ Pa |
| K_f | Bulk modulus of the fluid phase | 0.25 × 10 ⁹ Pa | 0.25 × 10 ⁹ Pa |
| G | Shear modulus of the frame | 4.00 × 10 ⁹ Pa | 3.57 × 10 ⁹ Pa |
| K_{fr} | Bulk modulus of the frame | 2.22 × 10 ⁹ Pa | 6.89 × 10 ⁹ Pa |
| k_0 | DC permeability | 10 ⁻¹² m ² | 10 ⁻¹⁶ m ² |
| η_f | Dynamic viscosity of the pore fluid | 10 ⁻³ Pa s | 10 ⁻³ Pa s |

Table 2. Material properties for the numerical simulation corresponding to the case study #2 for which the inclusion U2 is used to simulate a porous formation with oil. Following Linde *et al.* (2007) and Revil *et al.* (2007), the charge density of a partially water-saturated reservoir, \bar{Q}_V , should be replaced by \bar{Q}_V/S_W where S_W (unitless) represents the partial saturation in water.

| Parameter | Description | Unit U1 | Unit U2 |
|-------------|---------------------------------------|----------------------------------|----------------------------------|
| σ | Conductivity of the medium | 0.01 S m ⁻¹ | 0.001 S m ⁻¹ |
| \bar{Q}_V | Excess of charge per unit pore volume | 0.203 C m ⁻³ | 1585 C m ⁻³ |
| ρ_s | Bulk density of the solid phase | 2650 kg m ⁻³ | 2650 kg m ⁻³ |
| ρ_f | Bulk density of the fluid phase | 1000 kg m ⁻³ | 983 kg m ⁻³ |
| ϕ | Porosity | 0.25 | 0.33 |
| K_s | Bulk modulus of the solid phase | 36.5 × 10 ⁹ Pa | 37 × 10 ⁹ Pa |
| K_f | Bulk modulus of the fluid phase | 0.25 × 10 ⁹ Pa | 2.40 × 10 ⁹ Pa |
| G | Shear modulus of the frame | 4.00 × 10 ⁹ Pa | 5 × 10 ⁹ Pa |
| K_{fr} | Bulk modulus of the frame | 2.22 × 10 ⁹ Pa | 9.60 × 10 ⁹ Pa |
| k_0 | DC permeability | 10 ⁻¹² m ² | 10 ⁻¹¹ m ² |
| η_f | Dynamic viscosity of the pore fluid | 10 ⁻³ Pa s | 10 ⁻¹ Pa s |

signals by performing forward modelling of this contribution (see Ardjmandpour *et al.* 2011 for an example) using downhole measurements of the slowness and resistivity.

The geometry of the two synthetic case studies investigated later are shown in Fig. 2. The domain consists of a 600 m × 600 m region and is infinite in the strike direction (2.5 D assumption). In the first case study, the geometry is made of two half-spaces (U1 and U2) separated by a vertical interface located at $x = 300$ m. The seismic sources are located in Borehole #1 at $x = 100$ m and $z = 150$ m, 225 m, 300 m, 375 m, and 450 m for Shots #1, #2, #3, #4, and #5 respectively. In Borehole #2 (located at $x = 500$ m), we simulate an array of 50 sensors consisting of electrodes and geophones. The seismic sources are detonated sequentially in borehole#1. Meanwhile, seismic and electrical data are recorded for each individual seismic shot. Table 1 provides the material properties of media U1 and U2 used in the model.

Fig. 4 shows some snapshots of the seismic waves, the associated electrical current density and the resulting voltage at Electrode #25 in Borehole #2. Fig. 5 represents the signal at electrode #10 at location $z = 140$ m deep from the surface, which shows that seismoelectric signals are generated at the interface before the coseismic signal arrives at the receivers. While the coseismic signals show a characteristic hyperbolic shape, the seismoelectric signals arrive nearly instantaneously to all receivers. In the following, we call the ‘seismoelectric conversion (SC-) time window’ the time between the shot of the seismic source and the time of the seismic wave arrives at the receivers located in Borehole #2. The inverse problem involves locating the distribution of SC at the interface. It

will be described in the following sections using the data inside the SC-time windows for all the seismic shots.

4 FORWARD AND INVERSE MODELLING OF THE ELECTRICAL PROBLEM

Our main objective in this section is to estimate the spatial distribution of heterogeneities generating the seismoelectric source current, regardless of the values of the material properties themselves associated with these heterogeneities. At each time step, the seismoelectric signals recorded in Borehole #2 are like a self-potential profile (that is a distribution of voltages recorded at a set of electrodes with respect to a reference electrode and due to a quasi-static source of current). At each time in the SC-time window and for each shot, we use the electrical potential distribution recorded on the array of electrodes located in the second well in order to find the position of the current source generated through the SC between the two wells. At each time step, the inverse seismoelectric problem is therefore similar to a self-potential inverse problem for which several algorithms have been developed over the past few years using deterministic (Jardani *et al.* 2007; Minsley *et al.* 2007a, b; Jardani *et al.* 2008) and stochastic (Jardani & Revil 2009; Revil & Jardani 2010) approaches. In general, we want to invert these voltages to recover the position \mathbf{r} and amplitude of volumetric current source $\mathfrak{S}(\mathbf{r}, t)$. In our case, at each time step, the seismic waves impinging on the interface are responsible for the source current density, which has compact support (i.e. the spatial distribution of sources at any

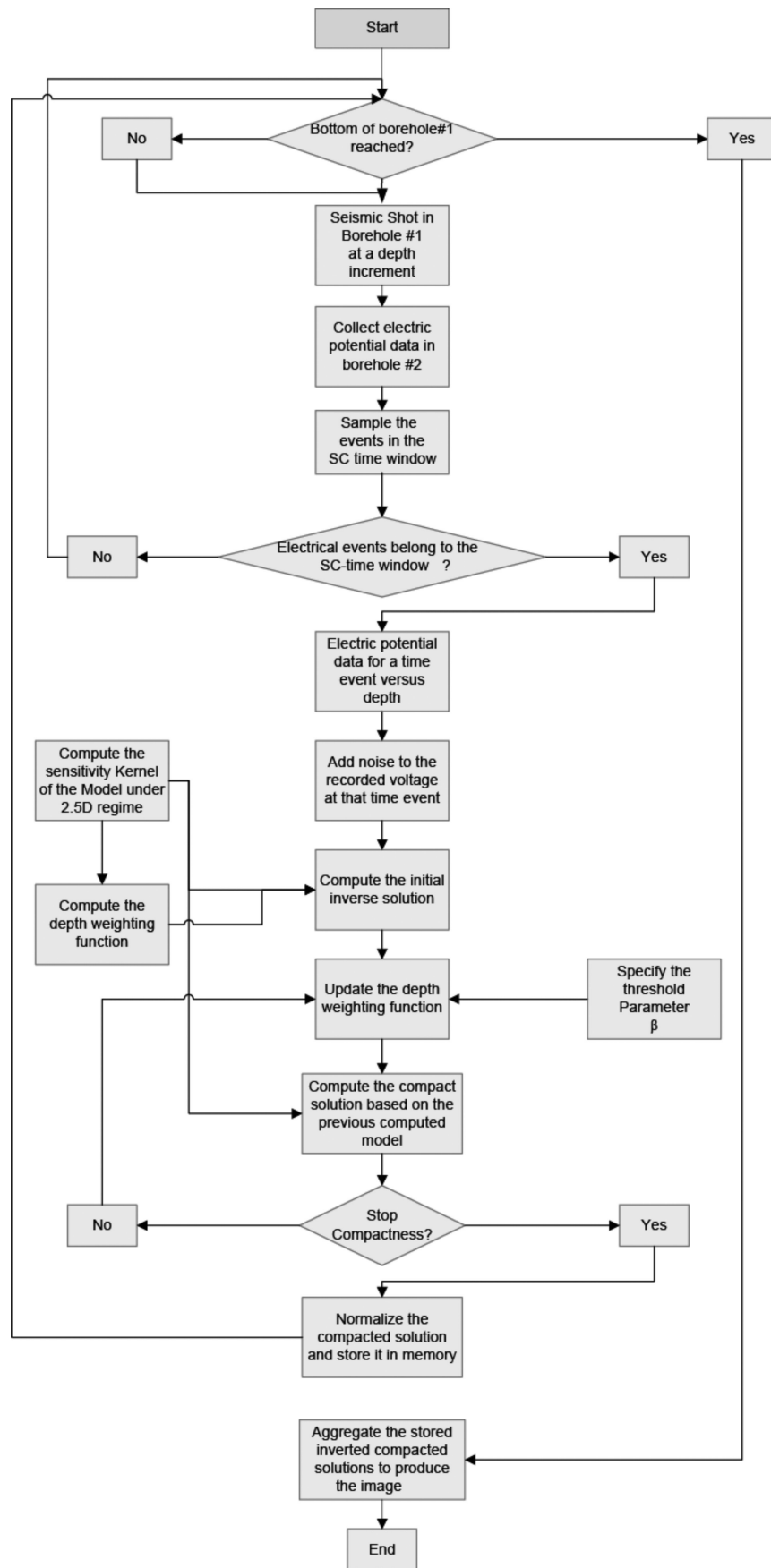


Figure 3. Flowchart of the seismoelectric forward and inverse modelling.

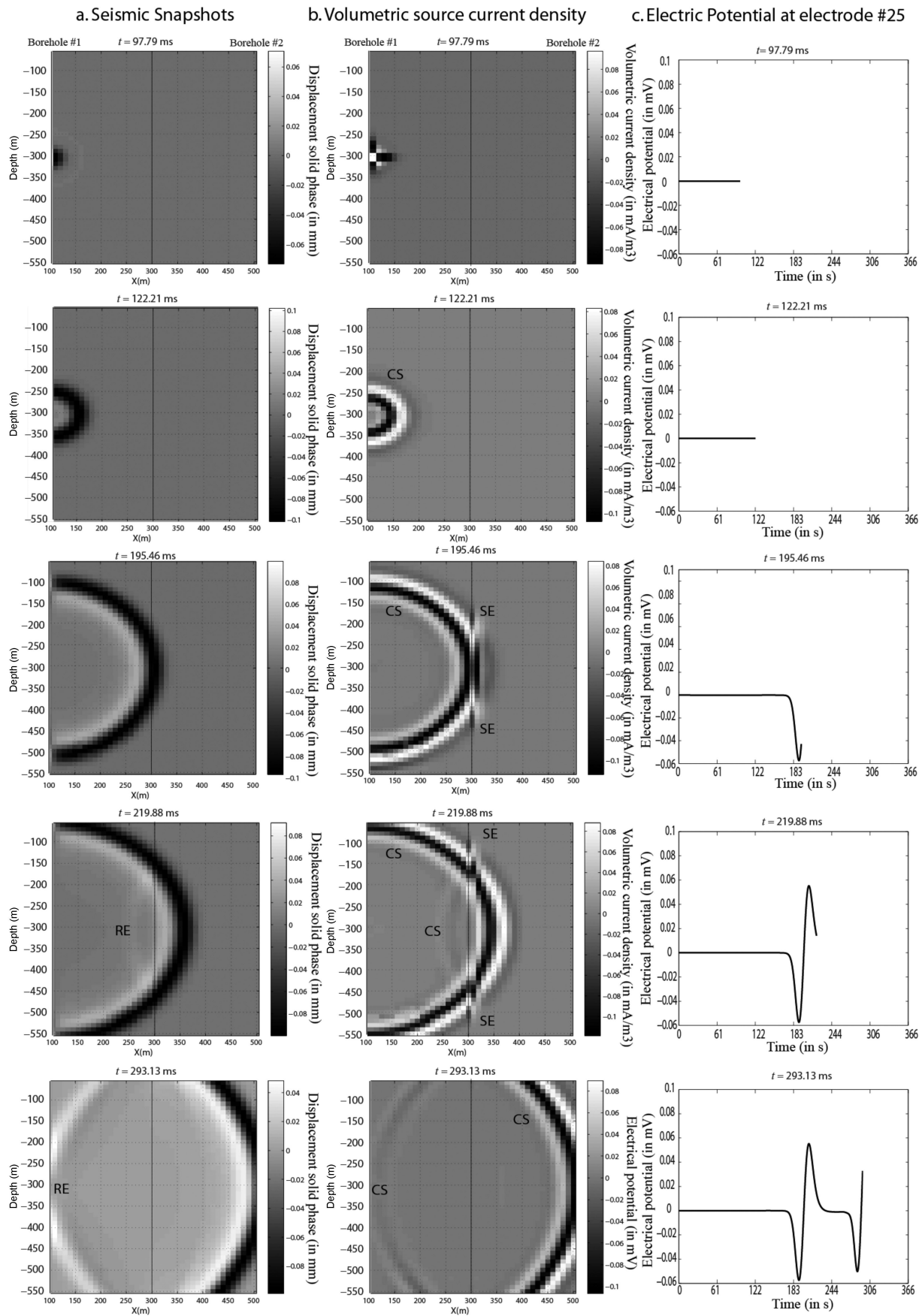
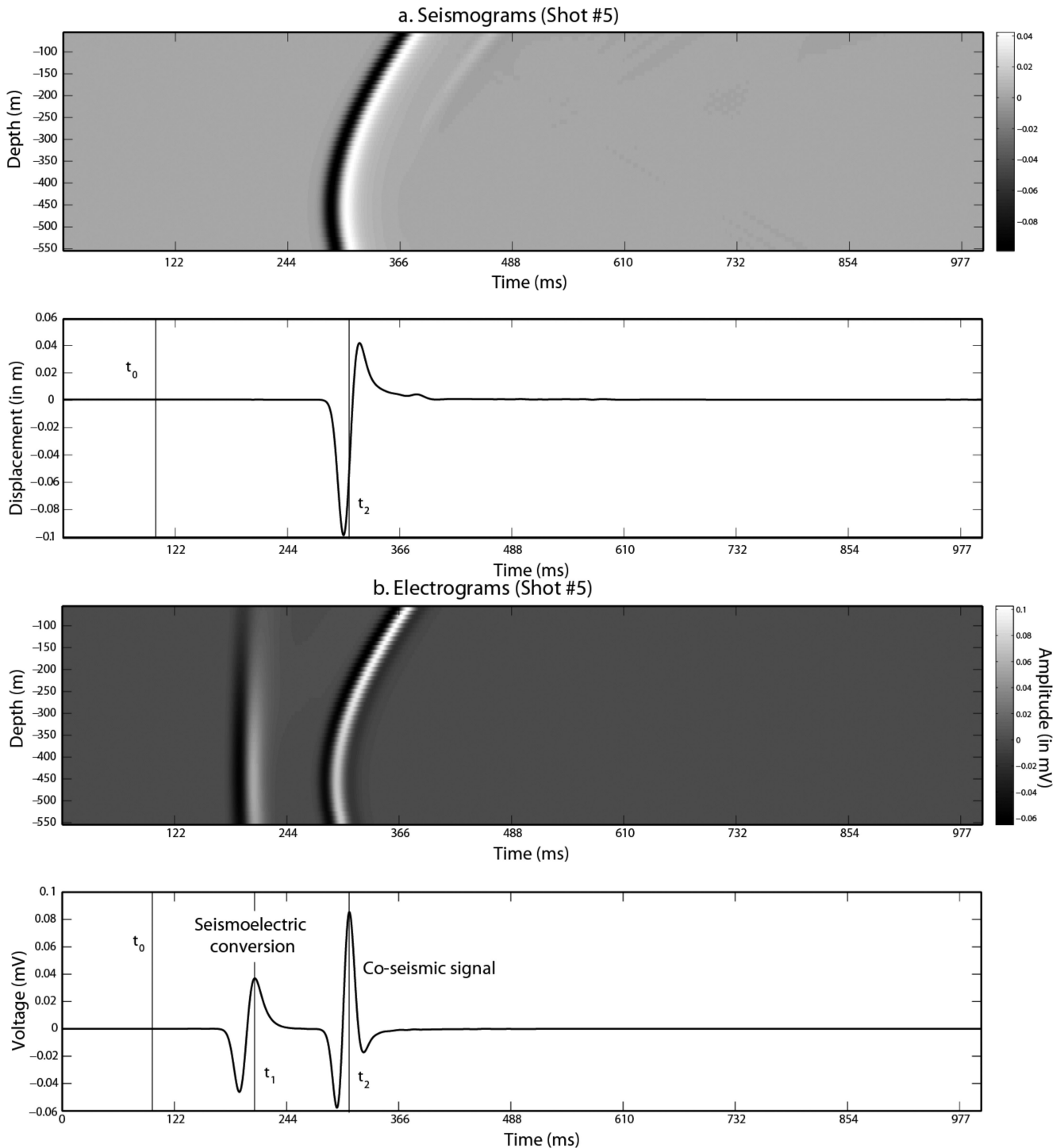


Figure 4. Modelling of the propagation of the seismic waves (displacement of the solid phase) and associated volumetric current density (Case Study #1, Shot #3). CS: Coseismic signals, SE: seismoelectric conversions, RE: reflected wave.



Downloaded from https://academic.oup.com/gji/article/188/3/1285/687427 by guest on 18 June 2021

Figure 5. Example of seismograms and electrograms corresponding to Shot #5 (deeper source). (a) Seismograms recorded in the offset borehole with a typical parabolic shape. An example of seismogram is given for geophone #25. (b) Electrograms recorded in the offset borehole showing the seismoelectric conversion at the vertical interface and the coseismic signal. An example of electrogram is given for electrode #25 (position $x = 500$ m, $z = 300$ m). The source occurs at $t = 110$ s.

given time is very sparse). Therefore, the algorithm we use below is based on compactness as a regularization tool as developed for the self-potential source inversion problem by Minsley *et al.* (2007a, b). A mathematical description of the algorithm is given later in Section 4.2.

We open now a small parenthesis to check analytically the validity of our numerical computations and to compute the size of

the first Fresnel zone for the seismic and seismoelectric problems. To estimate the time at which the SC occurs, we can estimate the P -wave velocity based on the material properties reported in Table 1. We obtain $c_p = 1935.5$ m s⁻¹ in unit U1 and 2163.5 m s⁻¹ in U2. Taking the geometry of Fig. 2 (Case Study #1), we obtain a traveltime of 0.115 s from the seismic source #5 to the interface and a traveltime of 0.213 s from the seismic source #5 to the geophone

#25. As the source has a time delay of $t_0 = 0.1$ s, the SC occurs at $t_1 = 0.215$ and the coseismic signal occurs at $t_2 = 0.313$ s. This is in agreement with the numerical results of Fig. 5. Using the relationship between the wavelength and the velocity of the P -waves $\lambda_s = c_p / f$ where f is the dominating frequency, the first Fresnel zone radius for the seismic wave is $r_s = (dc_p/2f)^{1/2}$. Using $d = 200$ m (Fig. 2), $f = 40$ Hz, $c_p = 1935.5$ m s⁻¹ in unit U1, we obtain $r_s = 69$ m. Using the relationship between the first seismic Fresnel zone and the seismoelectric Fresnel zone (see Section 2.5 earlier), we obtain $r_{SE} = 98$ m, which provides an idea of the lateral resolution of the seismoelectric method at this frequency.

4.1 2.5-D electric forward modelling

The Poisson equation governing the electrostatic potential distribution corresponds to eq. (26). The source term of this Poisson equation is described as a Dirac (delta) function and a point current source, I (in A), as suggested by Coggon (1971),

$$\mathfrak{S}(\mathbf{r}, t) = \nabla \cdot \mathbf{j}_s = I\delta(x - x_s)\delta(y - y_s)\delta(z - z_s), \quad (36)$$

where (x_s, y_s, z_s) denote the coordinates of the each point where the SC takes place. Two assumptions are made in order to transform the 3-D problem into a 2.5D problem. It is assumed that the model is homogenous in the strike direction y , that is, $\partial\sigma(x, y, z)/\partial y = 0$ and the strike direction extends to infinity in both directions. Solving the Poisson equation in the wave number domain, where k_y is the wave number in the strike direction, and using the Fourier cosine transform,

$$\tilde{\psi}(x, z, k_y) = \int_0^\infty \psi(x, y, z) \cos(k_y y) dy. \quad (37)$$

Eq. (36), in the wave number domain, takes the following form,

$$-\nabla \cdot (\sigma_{(x,z)} \nabla \tilde{\psi}(x, z, k_y)) + \sigma_{(x,z)} k_y^2 \tilde{\psi}(x, z, k_y) = I\delta(x - x_s)(z - z_s). \quad (38)$$

Therefore, the initial Poisson equation is transformed to a Helmholtz-type differential equation in the wave number domain. It is important to point out that the wave number is related to the model geometry and the separation distances between source and receivers. Eq. (38) is solved repeatedly for several wave numbers and then the solution is transformed from the wave number domain to the spatial domain following the approach taken by Dey & Morrison (1979) using an inverse cosine-transform.

In the finite element code COMSOL, the governing equation of the forward electrical model can be written at each time step as,

$$\mathbf{K}\psi = \mathbf{s}, \quad (39)$$

where \mathbf{K} is the kernel matrix that contains the discrete form of the differential operator on the left hand of eq. (39), \mathbf{s} is a vector containing the M source current density terms $\mathfrak{S}(\mathbf{x}, t)$, and ψ is the vector of electric potential observations at the N receivers locations.

At the boundaries of the domain, we used the following boundary conditions. A Neumann boundary condition is used at the interface between the model and the padding layer. At the outer edge of the padding layer, a Dirichlet's boundary condition is used. The electric potential at the outer edge of the padding layer tends to zero thus simulating an infinite domain (Dey & Morrison 1979).

4.2 The initial inverse solution

Because the number of the measurement points is much less than the number of mesh elements of the model where the source can be located ($N \ll M$) (this is typical of potential field problems), the inverse problem is underdetermined. It is also ill-posed and the solution is non-unique. The non-uniqueness of the inverse problem can be significantly reduced by using a regularization approach to select a solution that minimizes both the data misfit and, at the same time, carries a representation of the model structure that is consistent with some prior information (sparseness of the source distribution in this case).

The inverse problem involves reconstructing the spatial distribution of the volumetric source field [right-hand side of eq. (39)] at each time t through the optimization of the objective functions following the approach outlined by Minsley *et al.* (2007):

$$C = \|\mathbf{W}_d(\mathbf{G}\mathbf{s} - \psi^{obs})\|_2^2 + \lambda\|\Lambda\mathbf{s}\|_2^2, \quad (40)$$

$$\Lambda = \text{diag} \left[\sum_{i=1}^N G_{kj}^T{}^2 \right], \quad (41)$$

where $\mathbf{G} = \mathbf{PK}^{-1}$ denotes the Green's matrix ($N \times M$) computed as the product of the inverse kernel matrix times a sparse selector operator matrix \mathbf{P} ($N \times M$) that contains a single 1 on each row in the column that corresponds to the location of that receiver. The rows of \mathbf{G} can be computed effectively using reciprocity, which involves computing the forward response to a unit source located at each receiver. The vector Λ represents an inverse-sensitivity weighting function that accounts for distance from the receivers as well as the resistivity structure, \mathbf{s} is the vector containing the discretized source current density terms $\mathfrak{S}(\mathbf{r}, t)$ with dimension M , ψ^{obs} is the observed electric potential vector at the N sensors, and \mathbf{W}_d is a matrix that contains the information about the expected noise in the data. The parameter λ is a trade-off parameter between the two contribution of the cost function and is called the regularization term. This term balances the relative influence of the data misfit term, $C_d = \|\mathbf{W}_d(\mathbf{G}\mathbf{s} - \psi^{obs})\|_2^2$, and the model misfit term, $C_m = \|\Lambda\mathbf{s}\|_2^2$.

In the following, we consider \mathbf{W}_d to be diagonal with each element on the diagonal being the inverse of the estimated variance of the measurement errors. In all the tests, we consider a Gaussian noise with a standard deviation equal to 10 per cent of the computed data mean. This is a realistic noise level for this type of experiment accounting for the amplitude of the signals that are measured (see for instance Ardjmandpour *et al.* 2011). In addition, adding data weights helps to stabilize the inversion by eliminating artefacts that come from over-fitting the data.

The vector Λ represents the inverse-sensitivity weighting function. This function is needed because sensitivities decay quickly away from the receiver locations (typically as a power-law function of the distance from the receiver in a homogeneous medium, but is also affected by heterogeneous resistivity distributions). The weighting function is therefore needed to recover sources that are distant from the receivers.

Applying the following transform $\mathbf{s}_w = \Lambda\mathbf{s}$ and minimizing eq. (40) gives the equation,

$$[(\Lambda^{-1}\mathbf{G}^T\mathbf{W}_d^T\mathbf{W}_d\mathbf{G}\Lambda^{-1}) + \lambda\mathbf{I}]\mathbf{s}_w = \Lambda^{-1}\mathbf{G}^T\mathbf{W}_d^T\mathbf{W}_d\psi^{obs}. \quad (42)$$

The result of such an inversion is a smooth volumetric source current distribution. However, we know from the physics of the problem that the solution should be spatially compact. In the next

section, we describe a modification to the model regularization term that promotes this compactness.

4.3 Getting compact volumetric current source distributions

Source compactness is a relatively classical technique that suits the nature of the electrical problem because the volumetric source current densities associated with the SC tend to be spatially localized. The technique has been used in medical imaging and in geophysics (see for instance Last & Kubik 1983; Silva *et al.* 2001; and Minsley *et al.* 2007a; Minsley 2007). Compactness is based on minimizing the spatial support of the source. The new global objective function is modified to include compactness as a regularization term,

$$C = \|\mathbf{W}_d(\mathbf{G}\mathbf{s} - \psi^{obs})\|_2^2 + \lambda \sum_{k=1}^M \frac{s_k^2}{s_k^2 + \beta^2}, \quad (43)$$

where β is the threshold term introduced to provide stability as $s_k \rightarrow 0$. This form of the objective function is now non-linear since the compactness portion of the objective function is non-quadratic. The compactness term is effectively a measure of the number of source parameters that are greater than β , regardless of their magnitude. Minimization of this objective function, eq. (43), results in the solution that uses the fewest number of source parameters that are still consistent with the measured data, which enforces sparseness of the source distribution. As model values fall below the threshold β , they no longer contribute to the sum in eq. (43), and will be effectively masked from the solution.

In order to make this compact source problem linear so that it can be solved in a least-squares framework, and to incorporate the inverse sensitivity scaling, the model weighting operator $\mathbf{\Lambda}$ in eq. (40) is modified as

$$\mathbf{\Omega} = \text{diag} \left\{ \frac{\Lambda_{kk}^2}{s_{k(j-1)}^2 + \beta^2} \right\}, \quad (44)$$

where $\text{diag}(\cdot)$ extracts the diagonal elements of the argument. Hence the problem is transformed to a linear one by making the objective function quadratic in s_k by fixing the denominator of the model objective function $\mathbf{\Omega}$ with respect to the previous solution at step $(j-1)$ using an iteratively reweighted least squares approach. The vector \mathbf{s}_{j-1} is the initial model used to compute the first degree of compactness. A new vector $\mathbf{\Omega}$ is determined for every compactness degree based on the previous model generated from the immediate previous compactness degree. Using the renormalization with $\mathbf{s}_w = \mathbf{\Omega}\mathbf{s}$ and minimizing the global model objective function in eq. (43) gives us the iterative solution which utilizes compactness

$$(\mathbf{\Omega}_{j-1}^{-1} \mathbf{G}^T \mathbf{W}_d^T \mathbf{W}_d \mathbf{G} \mathbf{\Omega}_{j-1}^{-1} + \lambda \mathbf{I}) \mathbf{s}_{w,j} = \mathbf{\Omega}_{j-1}^{-1} \mathbf{G}^T \mathbf{W}_d^T \mathbf{W}_d \psi^{obs}. \quad (45)$$

The process is halted after several iterations. Focusing the image is a subjective choice. We found that nine iterations offers a good compactness level to localize the sources responsible for the observed self-potential data.

3.4 Benchmark tests

Before embarking into the process of inverting the seismoelectric signals generated by the seismoelectric forward model, it is essential to benchmark our inversion algorithm through a synthetic and well defined 2.5D electrical model. The benchmark model is a 450 × 500 m section described with 45 × 50 cells. The conductivity

distribution resembles that of the first case study of the vertical interface with two units U1 and U2 in the model. In the first test, we positioned a single point source at $x = 430$ m and $z = 310$ m and we recorded the electrical potentials at $x = 510$ m via an array comprised of 50 electrodes with 10 m vertical separation between adjacent electrodes so that the array extends from $z = 50$ m to $z = 550$ m. The initial inverse source solution is recovered using eq. (36), which is plotted in Fig. 6(a). This initial solution is diffusive and does not represent the spatial nature of the true compact source. Fig. 6(b) shows the electric potential corresponding to the source from the initial inverse solution versus the observed data with added noise. It is clear that the algorithm is able to predict, with a great accuracy, the measured voltages without overfitting the noise. Nevertheless, the 2-D representation of the model is overly smeared, thus the need to include compactness as a regularization tool as mentioned above. Upon performing only five iterations of eq. (45), the algorithm was able to locate the source precisely as shown in Fig. 6(b).

To test the ability of the algorithm to resolve two localized sources in a heterogeneous conductivity distribution, we conducted another benchmark test. Two volumetric current sources are located at position $(x, z) = (250$ m, 460 m) and (250 m, 150 m), respectively. The geometry is kept identical to the previous test. The resulting electrical voltage is aliased by the superposition of the two voltage distributions. The initial (diffusive) solution in terms of inverted current density is presented in Fig. 7(a) using the observed data contaminated with added Gaussian noise (same as above) and in Fig. 7(b), we show the result of the inversion after five iterations in the focusing procedure. The algorithm is able to distinguish and localize two distinct sources away from the receivers location without losing sensitivity. Also, the predicted electrical voltages recorded in borehole #2 [see Fig. 7(b)] is almost identical to the observed one. In other words, the algorithm is able to retrieve the true amplitude of the potentials without prior knowledge on the source.

These results highlight the ability of the compact source inversion to accurately recover the true spatial distribution of current sources. In these benchmark examples, the true sources are known to be highly compact. In other cases, the degree of compactness may not be known *a priori*. In other words, the electrical potential data can be accurately reproduced with diffuse or compact sources because of the non-unique nature of the problem, the user must decide how many compactness iterations is appropriate. The choice in focusing the tomogram is therefore the choice of the use, which is definitively a drawback of this approach. Our tests are showing that 5–10 iterations are usually a good iteration number to properly focus the tomogram. Future efforts to address this issue will include the use of auxiliary information from the recorded seismic response to help constrain the location of the heterogeneities.

5 CASE STUDIES

Our goal is to invert the source current densities at heterogeneities regardless of their magnitudes. However, we note that our algorithm is able to retrieve the values of the divergence of the current source density as well. Hence, inverting for these sources using recorded voltages in the offset borehole will provide us with a tool to distinguish and localize heterogeneities from the background material. We start by sequentially triggering seismic sources in the source borehole (Borehole#1) in order to produce electric potential time series recorded in Borehole#2 for times belonging to the SC-time window. The process is repeated for five seismic shots separated by

○ True position of the source One source localization problem

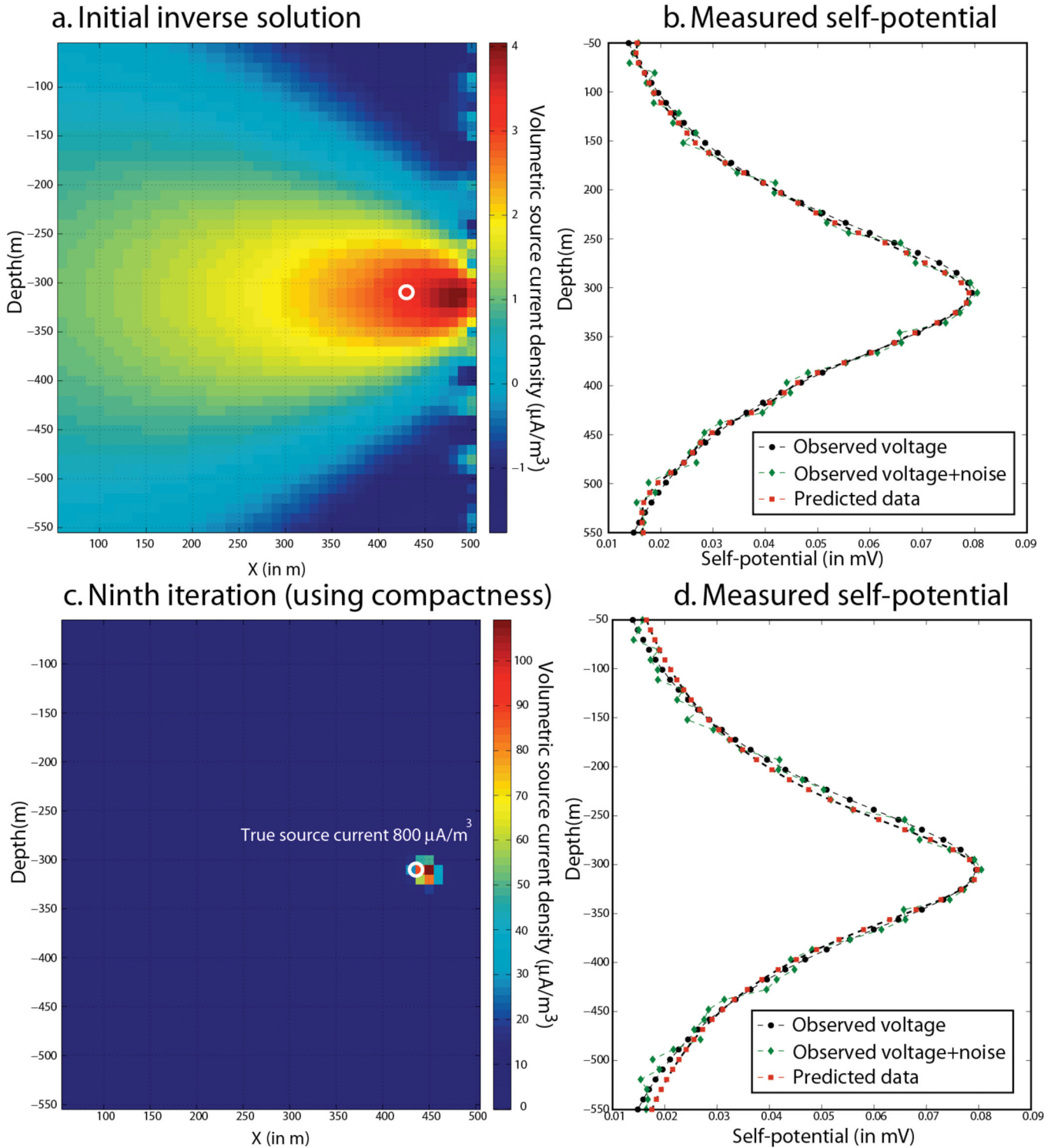


Figure 6. Test of the electrical source localization for a single source localized in an inhomogeneous medium. The resistivity distribution is given in Fig. 1(a) (see Table 1). A Gaussian noise with a standard deviation equal to 10 per cent of the computed data mean has been added to the data.

75 m in Borehole #1 (see Fig. 2). Electric potentials at each time event are recorded versus depth and processed by the inversion algorithm. As mentioned above, the decision to stop the compactness algorithm is arbitrary. It seems that focusing the tomograms up to the ninth iteration provides a suitable compact solution. All of the

inversions for different time events and for different seismic shots are aggregated to produce the final image, which shows the position of the heterogeneity between the two boreholes.

Fig. 8 shows eight voltage recordings as a function of depth for eight different time steps for shot#3 (middle of the source

○ True position of the source Two sources localization problem

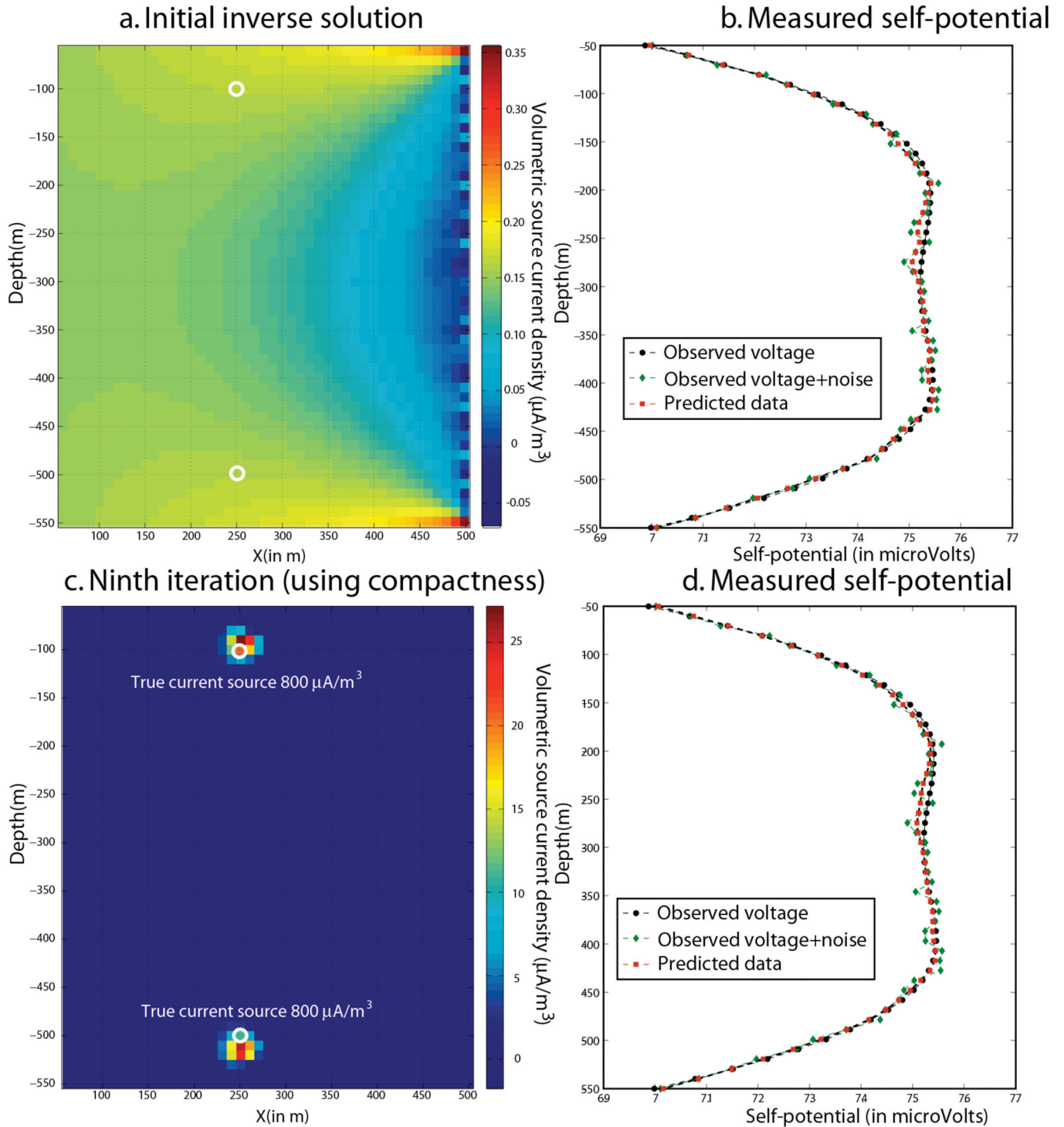


Figure 7. Test of the electrical source localization for two sources localized in an inhomogeneous medium.

borehole), corresponding to case study#1 in Fig. 2(a) (vertical interface between two porous media). The eight times we chose belong to the SC-time window, and sample the SC signal such as that illustrated in Fig. 5(b). At each time step, the vertical recordings of the potential field are processed using the source inversion algorithm to produce a snapshot of the seismo-electric generated source

on the interface, which is shown on a normalized scale in Fig. 9. Afterwards, the normalized source distributions at all time steps are aggregated to produce the tomogram presented in Fig. 10 that depicts the presence of a vertical interface at $x = 300$ m. The volumetric source current distributions are thresholded according to the global threshold level found by using Otsu method (Otsu 1979).

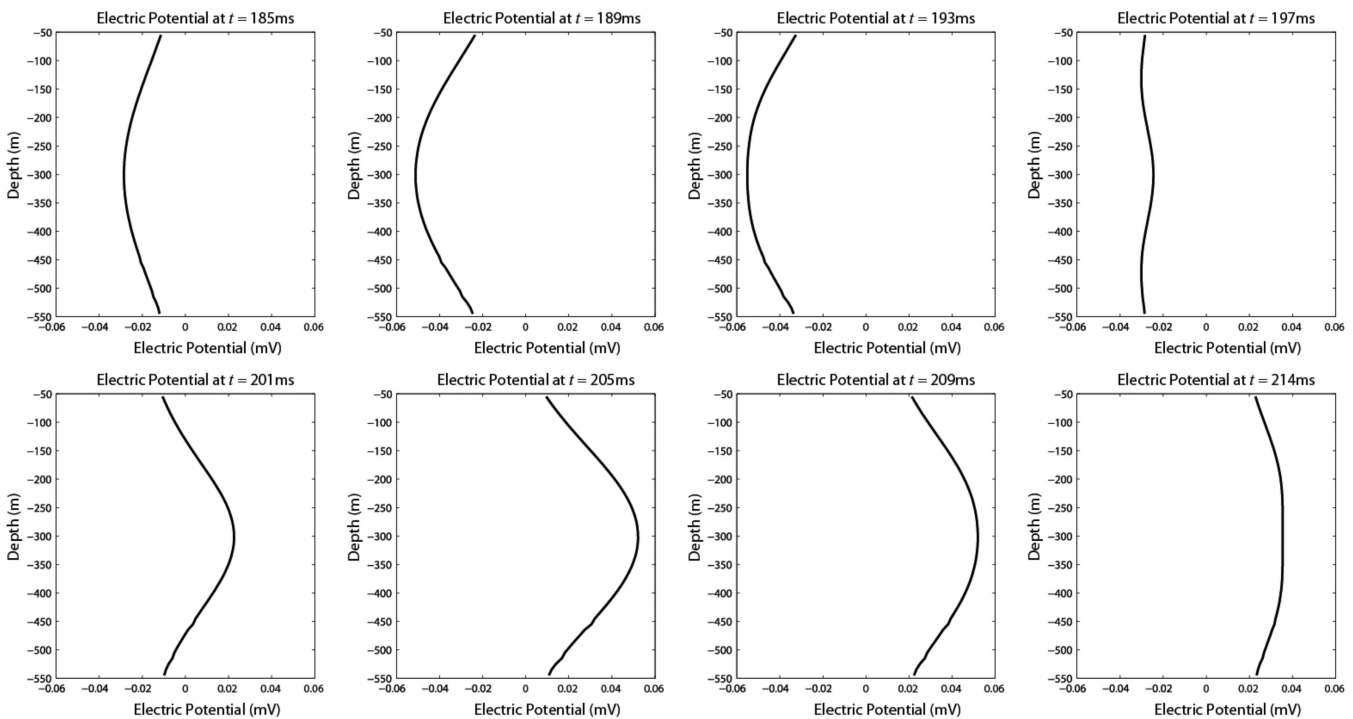


Figure 8. Vertical distribution of the electrical potential (in mV, reference at infinity) in borehole #2 at different times in the SC-time window in which the seismoelectric conversions taking place between the two boreholes occur (Shot #3).

This threshold is used to convert the distributions of the source current densities into a binary image by minimizing the interclass variance of the two types of pixels. Using multiple seismic shots enables us to ‘illuminate’ certain parts of the interface, which is usually the part closest to the source. Thus by utilizing several seismic shots along the source borehole, we were able to ‘illuminate’ the interface using the seismoelectric signals.

Another synthetic case study is demonstrated to highlight the ability of the algorithm to image reservoirs or oil plumes with irregular geometries for more realistic scenarios. In this case study we have an inclusion of a poroelastic material embedded in an homogeneous poroelastic material (Fig. 2b). The material properties of the two materials are those of Table 2. The same procedure is used as in the previous cases study and the tomogram produced is presented in Fig. 11, where we can relatively distinguish the inclusion from the background using seismoelectric data only.

As explained in the introduction, this work focuses on the localization of the current sources corresponding to the SC, but not the amplitude of these sources. In order to obtain an image of the localization of the seismoelectric sources, we aggregated all the sources for the five shots and for eight different time steps that sample the seismoelectric voltage distribution at the receivers. The resulting source localization, shown in Fig. 10, spreads around the position of the interface responsible for the SC. While the tomogram is not perfect, we think that this is a fair comparison between the position of the true interface and the image produced by the algorithm. Note the presence of few ghosts in the tomogram corresponds to spurious source localizations. The second case study investigates an ellipsoidal anomaly embedded into a homogeneous material. The final result (following the exact same procedure as for the first case study) is shown in Fig. 11. We see that the position of the anomaly is relatively well-localized, however, there are also few ghosts that are present in the tomogram.

6 DISCUSSION

In this section, we want to address few question that may arise regarding the applicability of the present methods. The first is related to the sensitivity of the approach to the choice of the source parameters. What happens indeed to the model outputs if we change the source characteristics? Our choice of the source parameters was to make the source as impulsive as possible. That said, the choice of the source is totally arbitrary and our approach is totally independent of the choice of the source. We can choose any type of source (e.g. a sweep), and we can always perform a deconvolution of the resulting seismoelectric signals with the (known) source in order to retrieve the impulse function of the system.

The second question we want to address is the noise level in the electrical data. Typically on land, it is easy to record the electrical field with a precision of at least one microvolt per meter and the precision on the measurements can be better than one nanovolt per meter for offshore applications (classically for CSEM) (Butler & Russell 1993; Mikhailov *et al.* 1997; Haines 2004; Dupuis *et al.* 2007). Therefore the signal-to-noise ratio adopted in this paper is rather pessimistic.

The third point is the use of compactness in the inversion of the electrical potential data, which is a typical inverse problem in potential field theory. The source inversion problem consist to identify the position of the source between the two wells. This principle is different from the inverse problem corresponding to the imaging of the material properties using a smoothness regularization approach. A complete analogous application of the method we used above has also been performed in the medical community using electroencephalographic (EEG) data (measuring time-varying electrical potentials on the scalp) and combining this information with resistivity information to spatially and temporally locate electrical sources within the brain. Portniaguine *et al.* (2001) proposed the compactness approach as a method to focus the position of the

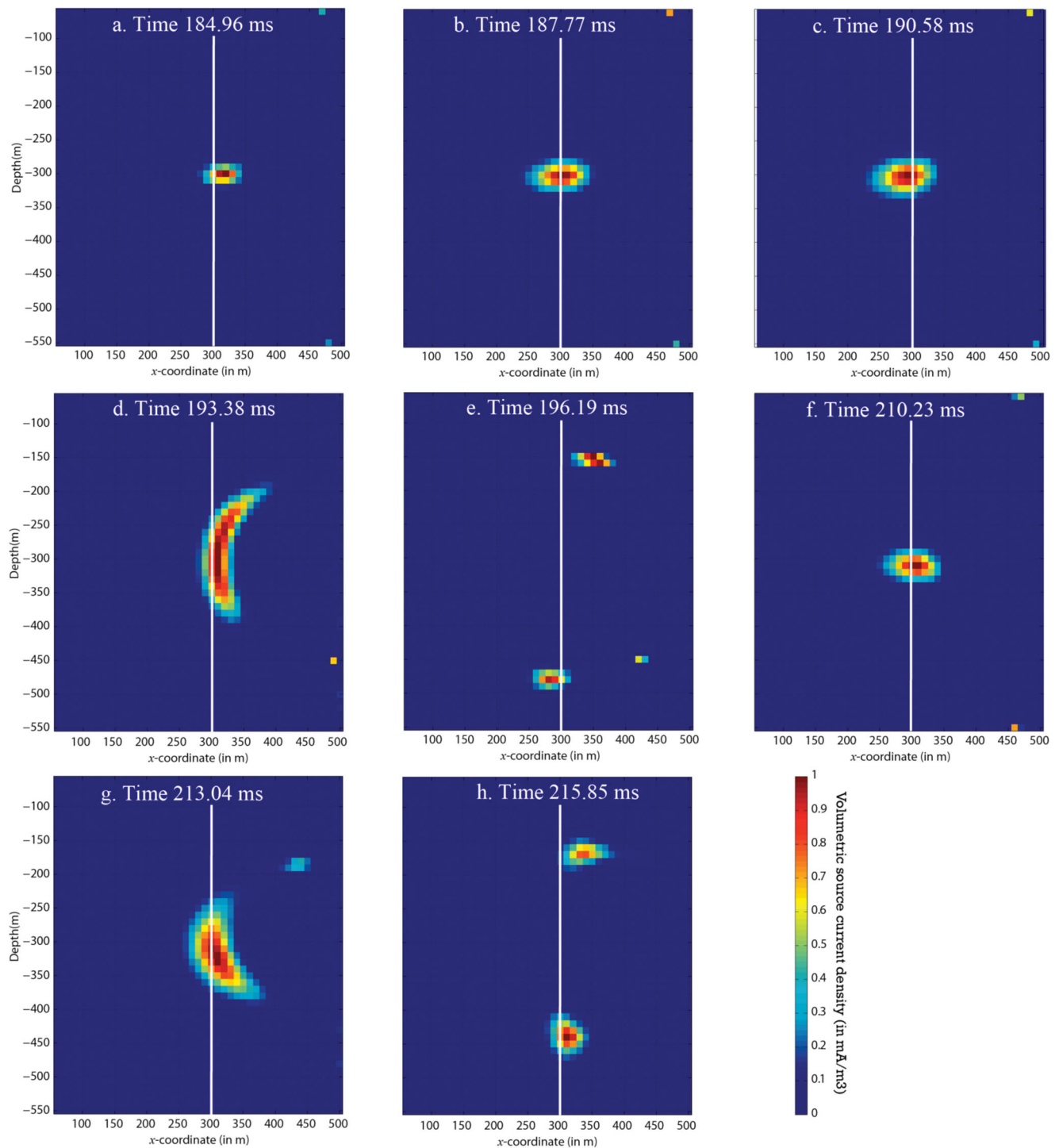


Figure 9. Source localization for the electrical potential distributions shown in Fig. 8 (shot #3). The white line indicates the position of the discontinuity between the units U1 and U2.

source responsible for the observed EEG anomalies. This approach has been very successful in EEG. We think that despite the drawback associated with the choice let to the user to stop the focusing of the tomogram, this method provides images that are more reliable than having only an unfocused image. The electrical signature collected at the boreholes due to SC is due the occurrence of local electrical source current densities like in EEG. Also we point out that the use of compactness does not remove the non-uniqueness of the inverse problem. As for other deterministic methods, this

approach provide a set of solutions on the location of the sources. The choice of the best solution is dependent on the availability of independent information, e.g. of a seismic nature.

7 CONCLUSIONS

We have presented the first cross-hole seismoelectric tomographic algorithm. Our inversion approach uses only the electrical information recorded in the observation borehole at each time step using

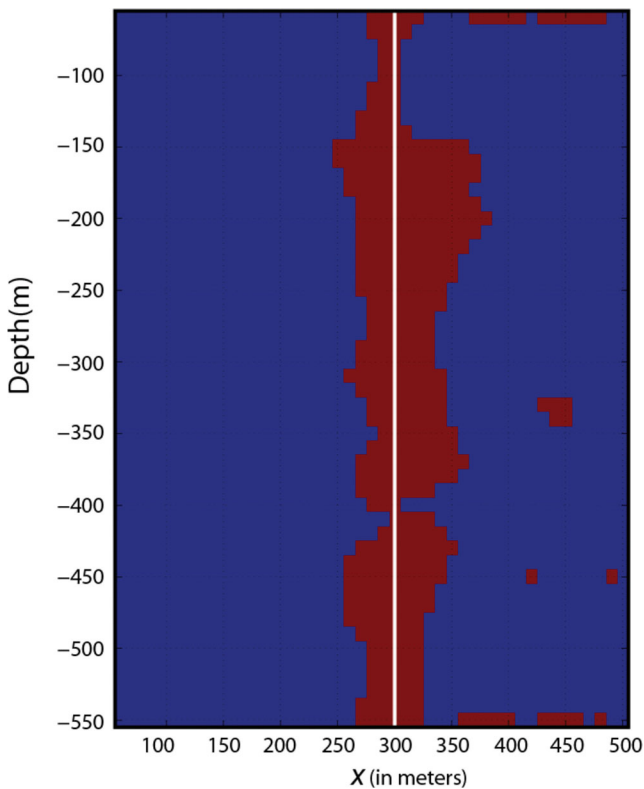


Figure 10. An aggregate of all the source distributions for the five shots using six characteristic times for each shot for the Case Study #1. The white line indicates the true position of the discontinuity.

realistic signal-to-noise ratios. Localization of the current sources is accomplished using knowledge of the resistivity distribution and incorporating compactness as a regularization tool. Errors in the source localization due to imperfect knowledge of the true resistivity structure are discussed by Minsley (2007, chapter 4). We demonstrated that we can approximately recover the position of heterogeneities using this approach. A more advanced approach could be to use the seismic information to estimate material properties and to provide additional constraint for the source localization. Indeed, if seismic tomography is first realized (using first arrival wave tomography for instance), a velocity model and its uncertainty can be recovered. Such a velocity model can be used to estimate where the wave is located at each time step. This location can subsequently be incorporated as a constraint for the areas where the SC occurs. This information could be used to help to remove the somewhat arbitrary choice of how many compactness iterations are needed for the source localization by providing additional constraints on the source localization. We could also use the magnetic information in the inverse problem as new magnetic sensors can be used in boreholes. As long as magnetic minerals are absent, the magnetic field is easier to invert than the electrical field as the magnetic permeability is constant at the opposite of the electrical conductivity.

ACKNOWLEDGMENTS

We would like to express our gratitude to Mike G. Loudin and the MENA Scholars Program at ExxonMobil Exploration Company (EMEC) for sponsoring AHA at the Colorado School of Mines during his Master's thesis. Funding was provided by the Petroleum Institute of Abu Dhabi to AR. We thank Seth Haines for fruitful discussions. Dr. T.K. Young is also thanked for his support at Mines.

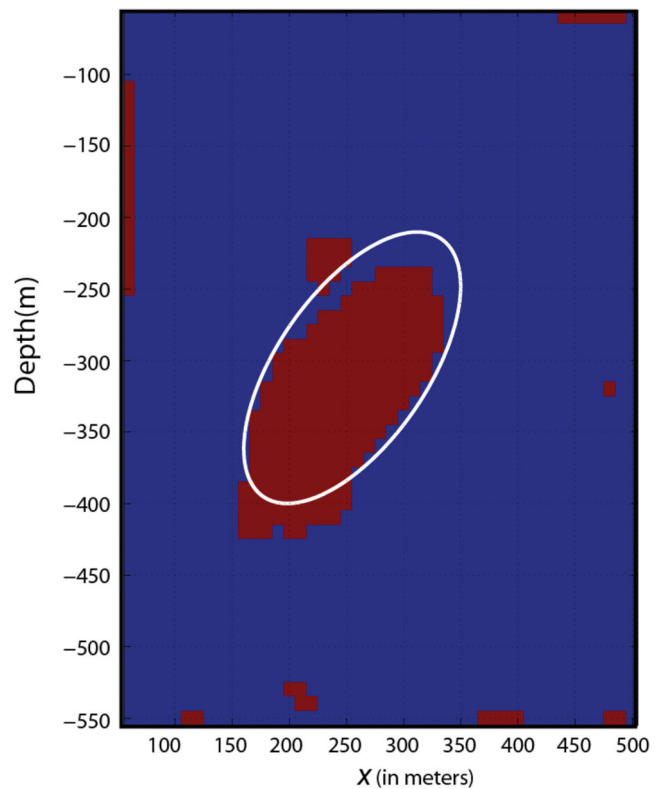


Figure 11. Aggregate of all the source distributions for the five shots using six characteristic times for each shot for the Case Study #2. The white line indicates the true position of the discontinuity between the materials U1 and U2.

We thank the Editor, Wolfgang Friederich, and two anonymous referees for constructive reviews.

REFERENCES

- Archie, G.E., 1942. The electrical resistivity log as an aid in determining some reservoir characteristics, *Trans. Am. Inst. Min. Metall. Eng.*, **146**, 54–62.
- Ardjmandpour, N., Pain, C., Singer, J., Saunders, J., Aristodemou, E. & Carter, J., 2011. Artificial neural network forward modelling and inversion of electrokinetic logging data, *Geophys. Prospect.*, **59**, 721–748, doi:10.1111/j.1365-2478.2010.00935.x.
- Biot, M.A., 1962a. Generalized theory of acoustic propagation in porous dissipative media, *J. Acoust. Soc. Am.*, **34**(9), 1254–1264.
- Biot, M.A., 1962b. Mechanics of deformation and acoustic propagation in porous media, *J. Appl. Phys.*, **33**(4), 1482–1498.
- Bolève, A., Revil, A., Janod, F., Mattiuzzo, J.L. & Jardani A., 2007. Forward modeling and validation of a new formulation to compute self-potential signals associated with ground water flow, *Hydrol. Earth Syst. Sci.*, **11**(5), 1661–1671.
- Bollhoefer, M., Grote, M.J., & Schenk, O., 2009. Algebraic multilevel preconditioner for the Helmholtz equation in heterogeneous media, *SIAM J. Sci. Comput.*, **31**(5), 3781–3805, doi: 1137/080725702.
- Butler, K.E. & Russell, R.D., 1993. Subtraction of powerline harmonics from geophysical records, *Geophysics*, **58**, 898–903.
- Coggon, J.H., 1971. Electromagnetic and electrical modeling by the finite element method, *Geophysics*, **36**, 132–155.
- Crespy, A., Revil, A., Linde, N., Byrdina, S., Jardani, A., Bolève, A. & Henry P., 2008. Detection and localization of hydromechanical disturbances in a sandbox using the self-potential method, *J. Geophys. Res.*, **113**, B01205, doi:10.1029/2007JB005042.

- Dai, N., Vafidiyas, A. & Kanasewich, E.R., 1995. Wave propagation in heterogeneous porous media: a velocity-stress finite-difference method, *Geophysics*, **60**, 327–340.
- Dahlen, F.A. & Tromp, J., 1998. *Theoretical Global Seismology*, Princeton University Press, Princeton.
- Dey, A. & Morisson, H.F., 1979. Resistivity modeling for arbitrarily shaped two-dimensional structures, *Geophys. Prospect.*, **27**(1), 106–136.
- Dukhin, A.S. & Shilov, V.N., 2010. The seismoelectric effect: a nonisochoric streaming current. 2. Theory and its experimental verification, *J. Colloid Interface Sci.*, **346**, 248–253.
- Dupuis, J.C. & Butler, K.E., 2006. Vertical seismoelectric profiling in a borehole penetrating glaciofluvial sediments, *Geophys. Res. Lett.*, **33**, L16301, doi:10.1029/2006GL026385.
- Dupuis, J.C., Butler, K.E., Kepic, A.W. & Harris, B.D., 2009. Anatomy of a seismoelectric conversion: measurements and conceptual modelling in boreholes penetrating a sandy aquifer, *J. geophys. Res.*, **114**, B10306, doi:10.1029/2008JB005939.
- Dupuis, J.C., Butler, K.E. & Kepic, A.E., 2007. Seismoelectric imaging of the vadose zone of a sand aquifer, *Geophysics*, **72**(6), A81–A85.
- Frenkel, J., 1944. On the theory of seismic and seismoelectric phenomena in a moist soil, *J. Phys. (Soviet)*, **8**(4), 230–241.
- Fourie, F.D., 2003. Application of Electrostatic Techniques to Geohydrological Investigations in Karoo Rocks, *PhD thesis*, University of the Free State, Bloemfontein, South Africa, 195 pp.
- Gao, Y. & Hu, H., 2010. Seismoelectromagnetic waves radiated by a double couple source in a saturated porous medium, *Geophys. J. Int.*, **181**, 873–896, doi: 10.1111/j.1365-246X.2010.04526.x.
- Garambois, S. & Dietrich, M., 2002. Full waveform numerical simulations of seismoelectromagnetic wave conversions in fluid-saturated stratified porous media, *J. geophys. Res.*, **107**(B7), doi:10.1029/2001JB000316.
- Gassmann, F., 1951. Über die elastizität poröser medien, *Vierteljahrsschr. Naturforsch. Ges. Zuerich*, **96**, 1–23.
- Haartsen, M.W. & Pride S., 1997. Electrostatic waves from point sources in layered media, *J. geophys. Res.*, **102**, 24 745–24 769.
- Haines, S.S., 2004. Seismoelectric imaging of shallow targets, *PhD thesis*, Stanford University, Palo Alto, CA, 191 pp.
- Haines, S.S., Klemperer, S.L. & Biondi, B., 2007. Seismoelectric imaging of shallow targets, *Geophysics*, **72**(2), G9–G20, doi:10.1190/1.2428267.
- Hu, H., Guan, W. & Harris, J.M., 2007. Theoretical simulation of electroacoustic borehole logging in a fluid-saturated porous formation, *J. Acoust. Soc. Am.*, **122**, 135–145.
- Huang, Q., 2002. One possible generation mechanism of coseismic electric signals, *Proc. Jpn. Acad.*, **78**(7B), 173–178.
- Huang, Q. & Liu, T., 2006. Earthquakes and tide response of geoelectric potential field at the Nijima station, *Chin. J. Geophys.*, **49**(6), 1745–1754.
- Hunt, C.W. & Worthington, M.H., 2000. Borehole electrokinetic responses in fracture dominated hydraulically conductive zones, *Geophys. Res. Lett.*, **27**, 1315–1318.
- Jardani, A. & Revil, A., 2009. Stochastic joint inversion of temperature and self-potential data, *Geophys. J. Int.* **179**(1), 640–654, doi:10.1111/j.1365-246X.2009.04295.x.
- Jardani, A., Revil, A., Bolève, A., Dupont, J.P., Barrash, W. & Malama, B., 2007. Tomography of the Darcy velocity from self-potential measurements, *Geophys. Res. Lett.*, **34**, L24403, doi:10.1029/2007GL031907.
- Jardani, A., Revil, A., Bolève, A., & Dupont, J.P., 2008. 3D inversion of self-potential data used to constrain the pattern of ground water flow in geothermal fields, *J. geophys. Res.*, **113**, B09204, doi:10.1029/2007JB005302.
- Jardani, A., Revil, A., Slob, E. & Sollner, W., 2010. Stochastic joint inversion of 2D seismic and seismoelectric signals in linear poroelastic materials, *Geophysics*, **75**(1), N19–N31, doi: 10.1190/1.3279833.
- Karpfinger, F., Müller, T.M. & Gurevich, B., 2009. Green's functions and radiation patterns in poroelastic solids revisited, *Geophys. J. Int.*, **178**, 327–337.
- Kepic, A.W., Maxwell, M. & Russell, R.D., 1995. Field trials of a seismoelectric method for detecting massive sulfides, *Geophysics*, **60**(02), 365–373.
- Kulesa, B., Murray, T. & Rippin, D., 2006. Active seismoelectric exploration of glaciers, *Geophys. Res. Lett.*, **33**, L07503, doi:10.1029/2006GL025758.
- Last, B.J. & Kubik, K., 1983. Compact gravity inversion, *Geophysics*, **48**(6), 713–721.
- Lathi, P.B., 1998. Modern Digital and Analog Integrated Communication Systems, *Oxford Ser. Elect. Eng.*, 401 pp.
- Linde, N., Jougnot, D., Revil, A., Matthäi, S.K., Arora, T., Renard, D. & Doussan, C., 2007. Streaming current generation in two-phase flow conditions, *Geophys. Res. Lett.*, **34**(3), L03306, doi:10.1029/2006GL028878.
- Martner, S.T. & Sparks, N.R., 1959. The electrostatic effect, *Geophysics*, **24**(2), 297–308.
- Migunov, N. & Kokorev, A., 1977. Dynamic properties of the seismoelectric effect of water saturated rocks, *Izvestiya, Earth Phys.*, **13**(6), 443–446.
- Mikhailov, O.V., Haartsen, M.W. & Toksoz, M.N., 1997. Electrostatic investigation of the shallow subsurface: Field measurements and numerical modeling, *Geophysics*, **62**(1), 97–105.
- Mikhailov, O.V., Queen, J. & Toksöz, M.N., 2000. Using borehole electrostatic measurements to detect and characterize fractured (permeable) zones, *Geophysics*, **65**(4), 1098–1112.
- Minsley, B.J., Sogade, J. & Morgan, F.D., 2007a. Three-dimensional source inversion of self-potential data, *J. geophys. Res.*, **112**, B02202, doi:10.1029/2006JB004262.
- Minsley, B.J., Sogade, J. & Morgan, F.D., 2007b. Three-dimensional self-potential inversion for subsurface DNAPL contaminant detection at the Savannah River Site, South Carolina, *Water Resour. Res.*, **43**, W04429, doi:10.1029/2005WR003996.
- Morency, C. & Tromp, J., 2008. Spectral-element simulations of wave propagation in porous media, *Geophys. J. Int.*, **175**, 301–345.
- Otsu, N., 1979. A threshold selection method from gray-level histograms, *IEEE Trans. Syst., Man, Cybernetics*, **9**(1), 62–66.
- Portniaguine, O., Weinstein, D. & Johnson C., 2001. Focusing inversion of electroencephalography and magnetoencephalography data, *J. Biomed. Technol.*, **46**, 115–117.
- Pride, S., 1994. Governing equations for the coupled electromagnetics and acoustics of porous media, *Phys. Rev. B*, **50**(21), 15 678–15 696.
- Pride, S.R. & Haartsen M.W. 1996. Electrostatic wave properties, *J. Acoust. Soc. Am.*, **100**(3), 1301–1315.
- Revil, A., 2007. Thermodynamics of transport of ions and water in charged and deformable porous media, *J. Coll. Interf. Sci.*, **307**(1), 254–264.
- Revil, A. & Jardani, A., 2010. Stochastic inversion of permeability and dispersivities from time lapse self-potential measurements: A controlled sandbox study, *Geophys. Res. Lett.*, **37**, L11404, doi:10.1029/2010GL043257.
- Revil, A. & Leroy, P., 2004. Governing equations for ionic transport in porous shales, *J. geophys. Res.*, **109**, B03208, doi: 10.1029/2003JB002755.
- Revil, A. & Linde, N., 2006. Chemo-electromechanical coupling in microporous media, *J. Coll. Interf. Sci.*, **302**, 682–694.
- Revil, A., Cathles, L.M., Losh, S., & Nunn, J.A., 1998. Electrical conductivity in shaly sands with geophysical applications, *J. geophys. Res.*, **103**(B10), 23 925–23 936.
- Revil, A., Schwaeger, H., Cathles, L.M., & Manhardt, P., 1999. Streaming potential in porous media. Part 2. Theory and application to geothermal systems, *J. geophys. Res.*, **104**(B9), 20 033–20 048.
- Revil, A., Leroy, P. & Titov, K., 2005. Characterization of transport properties of argillaceous sediments. Application to the Callovo–Oxfordian Argillite, *J. geophys. Res.*, **110**, B06202, doi:10.1029/2004JB003442.
- Revil, A., Linde, N., Cerepi, A., Jougnot, D., Matthäi, S.K. & Finsterle, S., 2007. Electrokinetic coupling in unsaturated porous media, *J. Coll. Interf. Sci.*, **313**(1), 315–327.
- Russell, R.D., Butler, K.E., Kepic, A.W. & Maxwell, M., 1997. Seismoelectric exploration, *Leading Edge*, **16**, 1611–1615.
- Silva, J.B.C., Medeiros, W.E., & Barbosa, V.C.F., 2001. Potential-field inversion: choosing the appropriate technique to solve a geologic problem, *Geophysics*, **66**(2), 511–520.

Zhu, Z. & Toksöz, M.N., 1998. Seismoelectric measurements in a fractured borehole model (expanded abstract), *Soc. Expl. Geophys.*, **BH2.7**, 314–317.

Zhu, Z., Haartsen, M.W., & Toksöz, M.N., 1999. Experimental studies of electrokinetic conversions in fluid-saturated borehole models, *Geophysics*, **64**, 1349–1356.

Zhu, Z. & Toksöz, M.N., 2003. Crosshole seismoelectric measurements in borehole models with fractures, *Geophysics*, **68**, 1519–1524.

Zhu, Z., Toksöz, M.N., & Burns, D.R., 2008. Electro seismic and seismoelectric measurements of rock samples in a water tank, *Geophysics*, **73**(5), E153–E164, doi:10.1190/1.2952570.